Journal of Colloid and Interface Science 617 (2022) 704–717

Contents lists available at ScienceDirect

Journal of Colloid and Interface Science

journal homepage: www.elsevier.com/locate/jcis

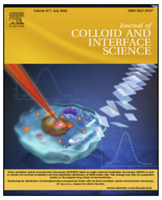

Glutathione-Triggered catalytic response of Copper-Iron mixed oxide Nanoparticles. Leveraging tumor microenvironment conditions for chemodynamic therapy

Javier Bonet-Aleta [a,b,c,1], Maria Sancho-Albero [a,b,c,d,1], Javier Calzada-Funes [a,b,c], Silvia Irusta [a,b,c], Pilar Martin-Duque [b,e,f,g], Jose L. Hueso [a,b,c,e,*], Jesus Santamaria [a,b,c,e,*]

[a] Instituto de Nanociencia y Materiales de Aragon (INMA) CSIC-Universidad de Zaragoza Campus Rio Ebro, Edificio I+D, C/ Poeta Mariano Esquillor, s/n, 50018 Zaragoza, Spain
[b] Networking Res. Center in Biomaterials, Bioengineering and Nanomedicine (CIBER-BBN), Madrid, Spain. Instituto de Salud Carlos III, 28029 Madrid, Spain
[c] Department of Chemical and Environmental Engineering, University of Zaragoza, Campus Rio Ebro, C/María de Luna, 3, 50018 Zaragoza, Spain
[d] Department of Molecular Biochemistry and Pharmacology, Istituto di Ricerche Farmacologiche Mario Negri IRCCS, 20156 Milan, Italy
[e] Instituto Aragonés de Ciencias de la Salud (IACS)/IIS Aragón, Avenida San Juan Bosco, 13, 50009 Zaragoza, Spain
[f] Fundación Araid. Av. de Ranillas 1-D, planta 2ª, oficina B, 50018 Zaragoza, Spain
[g] Present Address: Department of Surgery, University of Zaragoza Medical School; University of Zaragoza, Zaragoza, Spain

GRAPHICAL ABSTRACT

Bringing Glutathione down: Copper-Iron based nanoparticles play a determining catalytic role to favor Glutathione (GSH) depletion and subsequently generate reactive oxidative species (ROS) that pave the way for a promising ChemoDynamic Therapy based on the selective overexpression of redox active molecules especially in cancer cells.

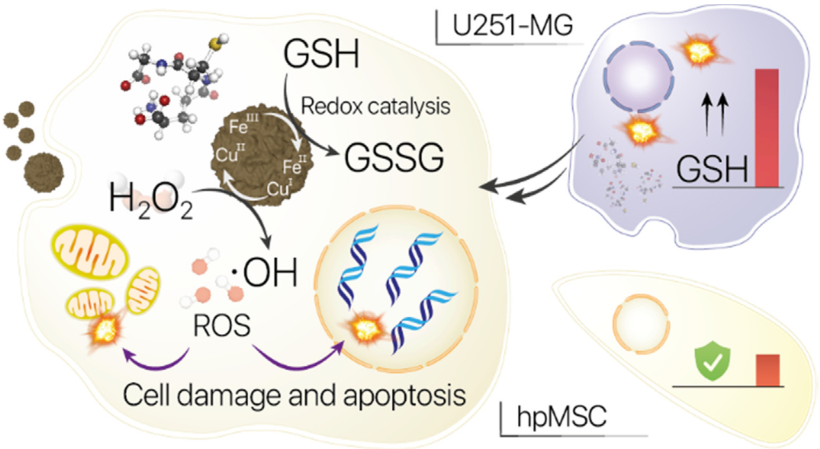

Abbreviations: GSH, Glutathione; ROS, Reactive Oxygen Species; TME, Tumor Microenvironment; CDT, Chemodynamic Therapy; GPX4, Glutathione Peroxidase; hpMSC, Human Placental Mesenchymal Stem Cells.

[*] Corresponding authors at: Instituto de Nanociencia y Materiales de Aragon (INMA) CSIC-Universidad de Zaragoza Campus Rio Ebro, Edificio I+D, C/ Poeta Mariano Esquillor, s/n, 50018 Zaragoza, Spain.

E-mail addresses: jlhueso@unizar.es (J.L. Hueso), jesus.santamaria@unizar.es (J. Santamaria).

[1] These authors contributed equally to this work.

https://doi.org/10.1016/j.jcis.2022.03.036

ARTICLE INFO

Article history:
Received 8 September 2021
Revised 8 February 2022
Accepted 8 March 2022
Available online 11 March 2022

Keywords:
Nanocatalysis
Cancer Therapy
Reactive Oxidative Species
Fenton reactions
Glutathione
Cascade Reactions

ABSTRACT

Heterogeneous catalysis has emerged as a promising alternative for the development of new cancer therapies. In addition, regarding the tumor microenvironment as a reactor with very specific chemical features has provided a new perspective in the search for catalytic nanoarchitectures with specific action against chemical species playing a key role in tumor metabolism. One of these species is glutathione (GSH), whose depletion is the cornerstone of emerging strategies in oncology, since this metabolite plays a pivotal regulatory role as antioxidant agent, dampening the harmful effects of intracellular reactive oxidative species (ROS). Herein, we present copper-iron oxide spinel nanoparticles that exhibit a versatile and selective catalytic response to reduce GSH levels while generating ROS in a cascade reaction. We demonstrate a clear correlation between GSH depletion and apoptotic cell death in tumor cells in the presence of the copper-iron nanocatalyst. Furthermore, we also provide a novel analytical protocol, alternative to state-of-the-art commercial kits, to accurately monitoring the concentration of GSH intracellular levels in both tumor and healthy cells. We observe a selective action of the nanoparticles, with lower toxicity in healthy cell lines, whose intrinsic GSH levels are lower, and intense apoptosis in tumor cells accompanied by a fast reduction of GSH levels.

1. Introduction

Despite intense research efforts in almost every branch of the natural sciences, cancer continues to be one of the leading causes of death worldwide [1]. Given the extensive panoply of oncologic treatments available, it is noteworthy that the use of heterogeneous catalysts has scarcely been explored until recent years. However, heterogeneous catalysts could in principle play two fundamental roles in cancer treatment: i) transform or destroy molecules that are essential for tumor growth and/or ii) generate toxic products in situ. Both effects, the depletion of useful metabolites and the generation of toxic species such as reactive oxidative species (ROS) have been the subject of a recent number of studies with different heterogeneous nanocatalysts delivered and activated in tumor microenvironments (TME) [2–5].

The metabolic differences between tumoral and healthy cells offer interesting opportunities for cancer therapy that can be leveraged with catalytic nanoparticles [6]. Notably, cancer cells possess a high dependence on ATP production to sustain their rapid proliferation [7] and exhibit an enhanced mitochondrial overproduction of ROS such as hydrogen peroxide (H_2O_2) or oxygen superanions ($^{\bullet}O_2^-$) [8–10] that are present in higher concentrations compared to normal cells [10]. In addition, H_2O_2 can be decomposed into highly reactive hydroxyl radicals. All of these species (H_2O_2, $^{\bullet}O_2^-$, $^{\bullet}OH$) may induce significant transformations in key biomolecules such as lipids, proteins or nucleic acids and lead to cell apoptosis [6,11]. In this regard, ChemoDynamic Therapy (CDT) exploits the decomposition of overproduced H_2O_2 through Fenton-like reaction catalyzed by transition metal-based nanoparticles (Fe, Co, Mn, Cu, Ni) to selectively induce apoptosis in cancer cells due to hydroxyl radical (•OH) generation [12–16].

However, the effectiveness of this strategy is often low, due to multiple challenges. In the first place, the concentration of intracellular H_2O_2 remains relatively low (i.e. 0.1–1.0 mM) [17,18] even for cancer cells, and therefore the capability of Fenton processes to yield $^{\bullet}OH$ is necessarily limited [6]. On top of that, the production of antioxidant molecules such as Glutathione (GSH) is upregulated in cancer cells [19] and this interferes with the products resulting from Fenton reactions, further preventing the effectiveness of ROS-triggered cancer treatments [13,20,21]. GSH is a natural tripeptide with ROS scavenging capacity and is mainly localized in the cytosol. Usual concentrations are in the range of 1–2 mM [22]. However, in some cell lines such as hepatocytes or malignant cancer cells this value can reach 10 mM [21,23,24]. The major role of GSH in cancer metabolism has been recognized for some time and has been linked to regulation of carcinogenic mechanisms as well as to cell proliferation and apoptotic processes [13,25–27]. However, understanding the intracellular mechanisms involving GSH remains elusive. This is likely hindering the development of new therapies, since the interplay between antioxidant molecules and ROS in the regulation of oxidative stress in cancer cells is central in the design of more effective CDT treatments [6,28]. Thus, while the modification of GSH metabolism has been proposed as a tool to enhance cell response to antitumoral drugs, this strategy is strongly limited due to its lack of specificity towards cancer cells, with potential side effects on healthy cells and tissues [21]. It is therefore not surprising that developing new ways to regulate GSH levels in tumor cells is being intensely investigated in recent years [27–29].

The main biochemical detoxification pathway of GSH is directly related with H_2O_2 [30] through the seleno-enzyme Glutathione Peroxidase (GPX4) [31]. H_2O_2 is able to oxidize the Se active center of the enzyme into Se-OH, which can react with GSH through its nucleophile thiol (-SH) group [32], forming a Se-SG intermediate (see Fig. 1). Then, another GSH molecule is able to establish a disulfide bridge with Se-SG, releasing GSSG, and regenerating the Se center. The process removes H_2O_2 and in doing so avoids the corresponding cell damage [32] (see Fig. 1). Because of this, reducing GSH levels has a direct impact on the capacity of cells to damp oxidative stress, and this has been exploited in CDT. Thus, recent investigations show how nanoparticles containing high-valence transition metals (Fe [28,33,34], Cu [35–37], Mn [29,34,38], Mo [36,39]) that are able to oxidize GSH can create a synergy that enhances the effect of CDT by promoting a scenario of lower GSH concentrations.

Fenton processes and GSH-depleting nanocatalysts can be connected through an oxidation–reduction catalytic cycle. Fenton-like reactions are typically catalyzed more efficiently by Fe(II) [40,41], Cu(I) [42,43] or Mn(II) [44] species, i.e. reduced transition metal elements, in comparison with their oxidized counterparts. A smart design of catalytic nanoparticles can successfully target the GSH/H_2O_2 system within the TME using cascade redox processes [17,29,35]. First, high-valence metal species are internalized inside cells reacting with GSH to yield oxidized GSH species (GSSG) and reduced-valence metal species (Fig. 1, bottom). Considering the faster Fenton kinetics [43,45,46] of reduced species, H_2O_2 molecules in the vicinity of the newly reduced metal will rapidly decompose yielding •OH while regenerating Mn + species, thus providing positive feedback to the catalytic cycle. This strategy leverages the comparatively high GSH [24,30,47] and H_2O_2

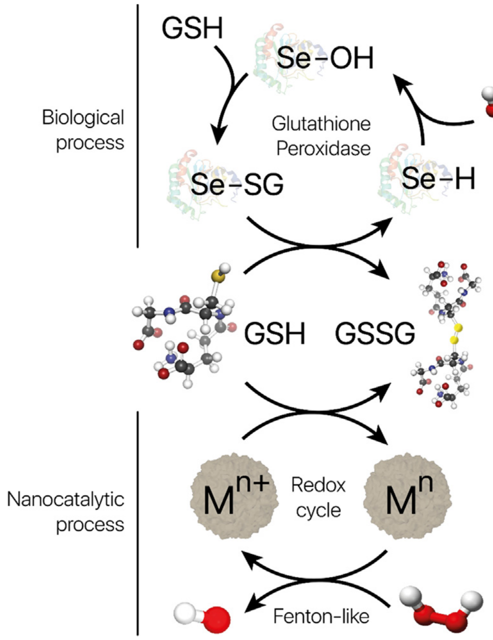

Fig. 1. Scheme depicting some key processes involving GSH: (Top) GPX4-catalyzed H_2O_2 removal through GSH oxidation into GSSG·H_2O_2 is able to oxidize Se-H active group from GPX4 yielding Se-OH. One GSH molecule is able to bind to Se-OH, forming Se-SG intermediate. Finally, another GSH molecule reacts with Se-SG releasing the final GSSG product. (Bottom) Catalytic redox process mediated by transition metal oxide nanoparticles. Electrons from -SH group of GSH GSH are able to reduce the oxidized metal specie (M^{n+}) to form active species in Fenton-like reaction (M^n). Once formed, Mn can decompose H_2O_2 into toxic ·OH radicals.

[17,18] levels inside tumor cells to couple GSH depletion and H_2O_2 decomposition processes.

Nevertheless, a study that not only correlates GSH levels in tumor and healthy cells but also relates these GSH concentrations to the performance of nanocatalysts has not been carried out. Encouraged by the possibilities arising from the above-described scenario, herein we have synthesized a copper-iron mixed oxide (CuFe) nanoparticle and evaluated its catalytic response in the presence of GSH, H_2O_2 and glucose. Furthermore, we have been able to develop an analytical protocol to accurately estimate GSH concentrations inside cells, demonstrating the high GSH concentrations levels in U251MG tumor cells in comparison with non-tumoral cell lines (i.e. human placental mesenchymal stem cells - hpMSC). This enabled us to establish for the first time a clear correlation between GSH levels and the catalytic capability to generate ROS while depleting GSH. Interestingly, our CuFe nanocatalyst is also able to trigger a parallel process of glucose oxidation, leading to a significant reduction of glucose levels, thus allowing the combination of CDT and starvation therapy, given the high glucose dependence of tumor metabolism. The results of the study shed light on the role played by GSH in the tumor environment and explain the enhanced response observed in the tumor cells after their exposure to CuFe NPs, in terms of their higher GSH content, suggesting the potential use of this catalyst nanoparticle to selectively induce tumoral cell death.

2. Results and discussion

2.1. Synthesis and characterization of the CuFe nanocatalyst

The synthesis of the Cu-Fe nanocatalyst uses Bovine Serum Albumin (BSA) as template (Fig. 2a). BSA favors the nucleation and growth of the CuFe nanoparticles thanks to the high density of carboxy, amino and thiol groups which can coordinate to Cu^{2+} and Fe^{3+} precursor ions to provide nucleation sites [48]. In addition, ethylene glycol (EG) was used as co-solvent, hindering the agglomeration between particles formed at nearby nucleation points, this and the large number of nucleation points contribute to the final distribution of small, well dispersed nanoparticles [49]. TEM and HAADF-STEM images show pseudo-spherical morphologies with a uniform diameter distribution (mean size of 7.8 ± 2.2 nm) (Fig. 2b to 2 g) and the random presence of some bigger nanoparticles in the 20–35 nm range (Fig. 2d-2i). NTA sizes were close to the 70 to 370 nm range (see Fig. S1a) indicating a limited degree of agglomeration in H_2O, while an even narrower dispersion in DMEM (Fig. S1b) was obtained. XRD analysis revealed the existence of a $CuFe_2O_4$ cubic spinel phase with the identification of (2 2 0), (3 1 1), (4 0 0), (5 1 1), (4 4 0) and (5 3 3) planes and a minor Cu cubic phase contribution (Fig. 2c). HRTEM images and FFT analysis of localized areas revealed lattice spacing of 0.148, 0.210 and 0.251 nm matching of the $CuFe_2O_4$ spinel with cubic phase, respectively [50,51] (Fig. 2h). EDS mappings further revealed a homogeneous distribution of Cu and Fe in the smaller nanoparticles (Fig. 2e) and the preferential presence of Cu surrounded by a sulfur-enriched outer layer in the bigger nanoparticles (Fig. 2j). Fourier Transform Infrared Spectroscopy (FTIR) reveals some characteristic features attributable to BSA in the purified catalyst, presenting bands at 2950, 1655 and 1395 cm^{-1} which can be attributed to Csp_3-H stretching, amide C═O stretching and C—N stretching, respectively [52,53] (Fig. 2k). XPS analysis corroborated the existence of the carbon surface species as shown in Fig. S2 where C—C/C═C, C—O and O-C═O contributions with Binding Energies (BEs) centered at 284.5, 286 and 288.8 eV were identified [54]. XPS also confirmed the presence of highest valence states for Fe(III) and Cu(II) catalytic species (Fig. 2l-2 m). X-ray photoemission peaks of the Cu2p revealed the major presence of Cu^{2+} species with binding energies of 933.7 eV and well defined satellite shakeups at 940–945 eV [55,56]. It is also worth mentioning the presence of a minor fraction (12 %) of either monovalent or metallic Cu, attributable to the lower binding energy a second contribution at ca. 932 eV [55,56]. Likewise, the analysis of the Fe2p region revealed a combination of Fe^{2+}/Fe^{3+} valence states with peaks centered at 710.5 eV and 712.4 eV attributable to Fe 2p3/2 orbitals of Fe^{3+} and Fe^{2+}, respectively [57,58]. The presence of satellite peaks at 715 and 719.8 eV corroborated the existence of both oxidation states [57,58] (see Tables S1-S2).

2.2. CuFe catalytic activity towards GSH depletion and GSH quantification

The presence of high-valent oxidation states in the surface (Fe^{III} and Cu^{II}) confers the possibility of promoting the oxidation of reducing molecules such as GSH. This would be highly interesting as it would deplete GSH levels inside the cell while at the same time yielding Fe(II) and Cu(I), species that are active in Fenton reaction, reacting with H_2O_2 to yield hydroxyl radicals (·OH), as depicted in Fig. 1. Thus, the first step in the proposed cascade-reaction consisted in the catalytic oxidation of GSH by CuFe. The capabilities of CuFe regarding GSH depletion were evaluated using a benchmarking assay with 5,5′-Dithiobis(2-nitrobenzoic acid (DNTB). DNTB represents a dimer of TNB linked by a S—S bond. In the presence of GSH (in a pH range between 7 and 8), this S—S bond is broken yielding TNB as product, which is easily detectable thanks to its absorption at 412 nm (Fig. S3). In fact, catalytic GSH oxidation experiments described in the literature typically use spectroscopic analysis (via UV–vis) to follow the reaction indirectly through analysis of TNB^{2-} [28,36,59–61].

However, while this kind of analysis is valid to establish a proof of concept, it remains insufficient to quantify GSH concentration

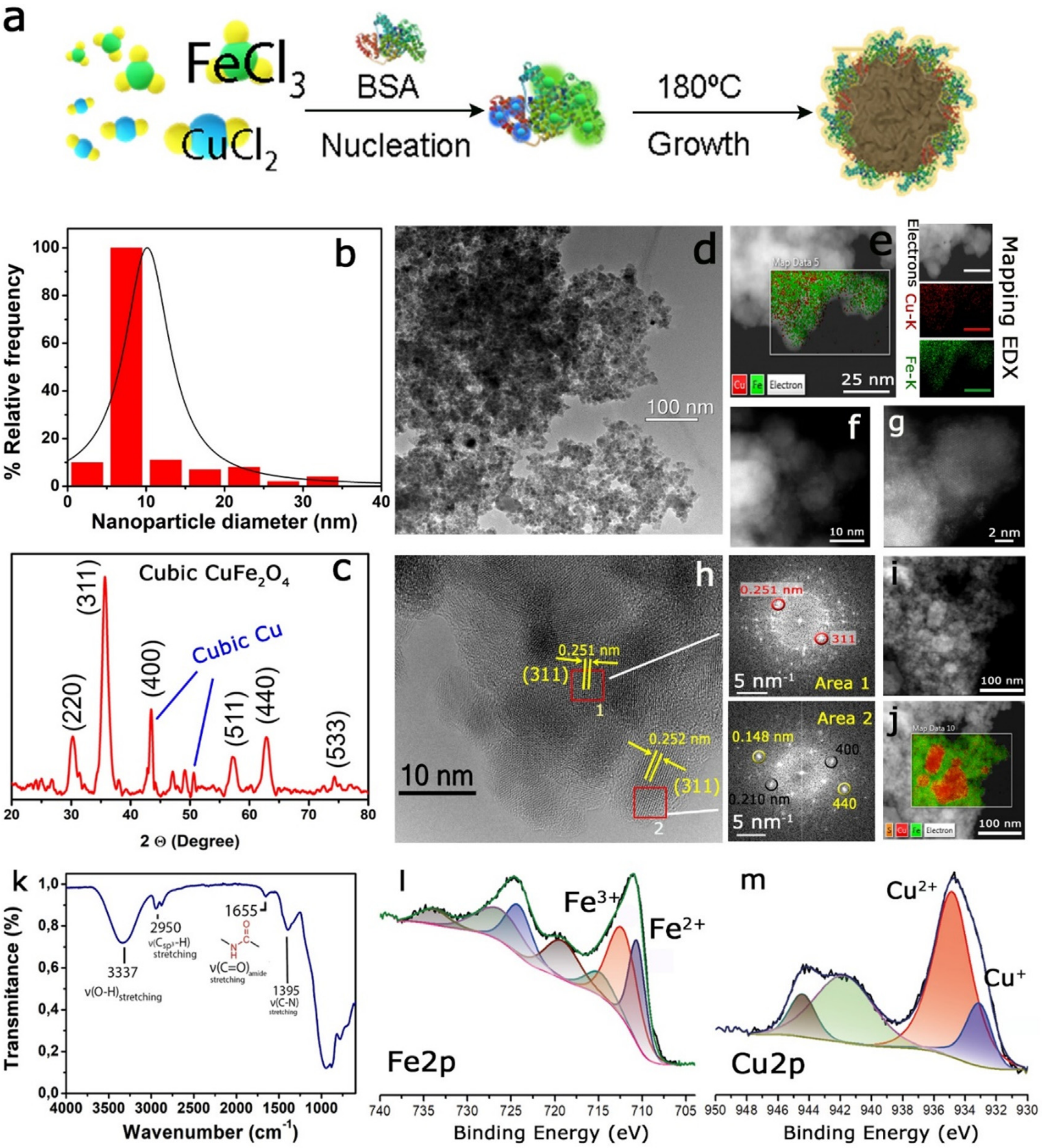

Fig. 2. Morpho-chemical characterization of the Cu-Fe nanoparticles: (a) Synthesis scheme of CuFe nanocatalyst using BSA as template The coordination of Cu^{2+} and Fe^{3+} cations to BSA functional groups generates a host of polymer-bound nucleation sites which provide a controlled and homogeneous growth of the particle; (b) Particle size distribution based on TEM image analysis with imageJ software (n = 150); (c) XRD pattern of CuFe nanoparticles attributable to a predominant cubic spinel phase of $CuFe_2O_4$ and a secondary phase of Cu; (d) Low magnification TEM image of the CuFe nanoparticles; (e) HAADF-STEM image and EDS elemental mappings corresponding to the Fe-K and Cu-K intensities and distributions; (f)-(g): High resolution HAADF-STEM images accounting for the crystallinity of the nanoparticles; (h) High resolution TEM images of the CuFe nanoparticles and corresponding FFT in selected areas (marked with red squares with the identification of lattice spacings matching to (3 1 1), (4 0 0) or (4 4 0) planes of $CuFe_2O_4$; (i) STEM image accounting for the presence of 20–35 nm nanoparticles; (j) EDS elemental mapping of (i) accounting for the preferential presence of Cu and an outer layer of S in the bigger nanoparticles; (k) FT-IR spectrum exhibiting characteristic BSA bands; (l) X-ray photoemission spectra (XPS) corresponding to Fe2p region; (m) X-ray photoemission spectra (XPS) corresponding to Cu2p region; Binding Energies and fitting assignations can be found in the Supplementary Information.

with time due to: (1) Difficulties to obtain an accurate calibration curve that allows precise determination of intracellular GSH and (2) Overlapping between DTNB and TNB^{2-} signals. To overcome these drawbacks, in this work we have established a quantification protocol using UPLC-PDA (see Experimental Section for details). We observed that our CuFe nanoparticles were able to convert a large proportion (up to 70% under the conditions tested) of the GSH at room temperature, even in the absence of H_2O_2 (see Fig. 3a). The addition of H_2O_2 increased the GSH conversion levels to up to 85% only in the presence of the CuFe catalyst (Fig. 3a). XPS analysis after reaction (Fig. S4 and Table S3) confirmed the generation of reduced Fe(II) and Cu(I) species on the catalyst as previously claimed by Liu et al.[28] and Hu et al. [61] with Cu-Fe based nanocatalysts. For Cu-based nanoparticles, literature reports show a clear reduction of Cu(II) to Cu(I) after GSH reaction [35,61]. Interestingly, in contrast with the strong reduction detected in the Cu(II) species, Fe(III) species are still present after 1 h of GSH reaction, although a clear decrease of the Fe^{3+}/Fe^{2+} ratio can be observed. It is reasonable to assume that GSH-oxidation is preferentially occurring via interaction with Cu(II) sites than with Fe(III), in agreement with the lower redox potential of Cu^{2+}/Cu^{+} (0.16 V) in comparison with Fe^{3+}/Fe^{2+} potential (0.77 V). The newly reduced

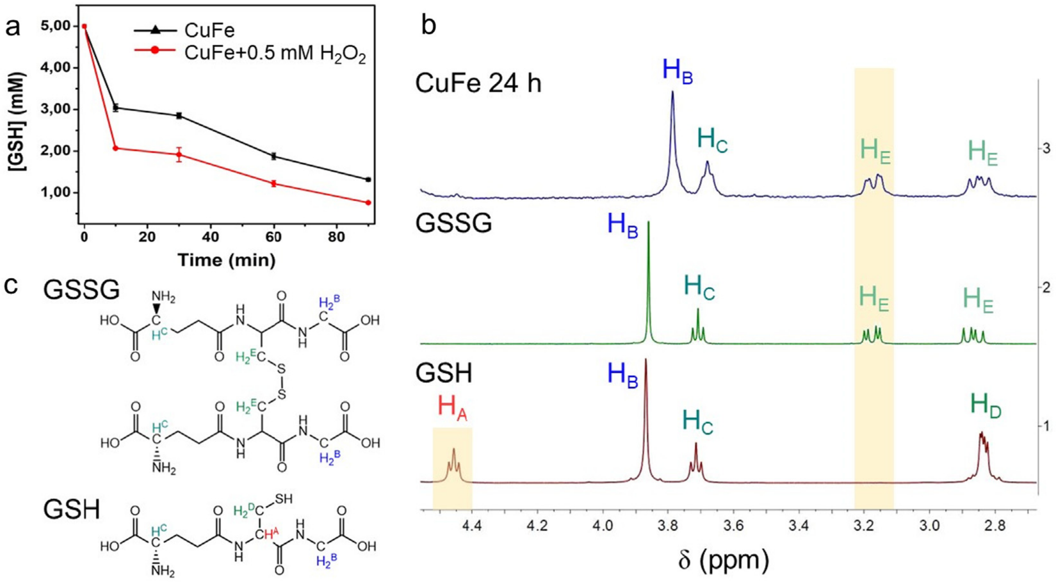

Fig. 3. GSH-depletion capabilities of CuFe nanoparticles and detection of GSH and GSSG by NMR spectroscopy: (a) Evolution of GSH in the presence of CuFe in the absence and in the presence of H_2O_2; No GSH conversion was detected in the absence of the CuFe catalyst (n = 3), Reaction conditions: [Catalyst] = 0.1 mg·mL^{-1}, $[GSH]_0$ = 5 mM, $[H_2O_2]_0$ = 0.5 mM, total volume of reaction = 2.5 mL;; (b) ^{1}H NMR spectra of GSH, GSSG and GSH + CuFe after 24 h; Reaction conditions: [Catalyst] = 0.1 mg·mL^{-1}, $[GSH]_0$ = 5 mM, total volume of reaction = 2.5 mL; (c) Molecular structures of GSH and GSSG with the corresponding signal assignment.

species are prone to undergo Fenton reaction with H_2O_2 to produce ·OH radicals and regenerate Fe(III) and Cu(II) species, thereby enhancing its catalytic response (see also Fig. 4 below).

Furthermore, Fenton-like response is more favored at higher pH values for Cu than for Fe catalysts [62,63]. In this study, in addition to GSH depletion, we have also studied the formation of the main reaction product (GSSG) using ^{1}H NMR analysis of the reaction medium (Fig. 3b-3c). It can be seen that GSH characteristic chemical shifts (4.45 ppm, Cys-CH; 2.83 ppm, Cys-CH_2) disappeared after 24 h of incubation with CuFe. The newly formed peaks (3.17 ppm, Cys-CH_2; 2.86 ppm, Cys-CH_2) matched with GSSG signals [64,65]. Wang et al. [61] found this analogous reaction product (GSSG) with Cu-hexacyanoferrate nanoparticles. However, no further studies of reaction product have been performed with Fe(III) species. Taking into account that no additional signals are found in the ^{1}H NRM spectra, it can therefore be concluded that Fe(III)-assisted GSH catalysis yields GSSG as product (Fig. 3c).

2.3. Evaluation of catalytic ·OH generation

To confirm the generation of reactive species derived from Fenton-like reactions, a systematic evaluation was carried out via MB assay [29,66]. At lower pH values (pH = 4.5, AcONa/AcOH buffer), CuFe NPs can promote methylene blue oxidation through Fenton processes (Fig. 4a, scenarios 1–3) in comparison with neutral pH (7.0, PBS) (Fig. 4a, scenarios 4–6), where the reaction is negligible in the absence of GSH. The main representative reactions are presented in Fig. 4e-f. In the absence of GSH (Fig. 4e), H_2O_2 must act as reducing agent of Fe(III) and Cu(II) (Reactions 1–2 and 4, respectively). Fe^{2+} is the active iron specie in Fenton reaction responsible of producing ·OH (Reaction 3), yielding Fe^{3+} as product [40,41]. However, the generation of Fe^{2+} is hampered by slow kinetics and this retards the continuous production of $^\bullet$OH [41]. In the case of Cu, a similar trend is also found with the pair Cu^+/Cu^{2+} [42,43]. Nevertheless, the characteristic tumoral environment offers a large GSH concentration [24,47] and this enables an alternative mechanism to take place. This antioxidant molecule with $E_0 < 0$ mV [67] can act as an accelerator for the generation of Cu^+ [35] and Fe^{2+} [34] species.

These Fe(II) and Cu(II) species formed in reactions 2 and 4 readily react with intracellular H_2O_2 (reactions 3 and 5) yielding ·OH radicals that quickly react with MB, dramatically enhancing the reaction rate compared to the process in the absence of GSH (Fig. 4-a-4b). An alternative ·OH detection method with sodium terephthalate (NaTA) was also employed to validate the generation of ROS via a Fenton-like mechanism (Fig. S5) [60]. Interestingly, the concentration of GSH outside cancer cells is much lower, down to μM levels [68] and this is low enough to avoid triggering this cascade reaction outside the cell (Fig. S6). In general, GSH concentration in cell cytosol have been found to be heterogeneous being present in millimolar concentrations (varying from 1 to 10 mM) [69]. However, in normal and healthy cells, GSH levels range from 1 to 2 mM. For instance, in red blood cells, GSH concentrations vary from 0.4 to 3 mM [70]. In the case of the brain, GSH concentrations have been described to be approximately 1.5–3 mM) [71]. Nevertheless, some cell types such as hepatocytes (whose role is to export GSH) the concentration of intracellular GSH can even reach 10 mM, a concentration comparable to the GSH levels in cancer cells [22]. Also, discrepancies in GSH levels have also been observed in tumoral areas, depending on the tissue under study. GSH has been shown to be elevated in breast, ovarian, head and neck and lung cancer, but lower in brain and liver tumors, in comparison to normal tissue [20]. Therefore, the analysis of the GSH levels should performed in every organ and tissue comparing to their disease-free controls, as it has been discussed whether the tumor might induce changes in glutathione in nearby disease-free peritumoral tissue.

Ma et al. [35] also reported cascade reaction with Cu-cysteine nanoparticles employing 0.5 mM GSH to in situ generate Cu(I) active species that could then react with H_2O_2. It is noteworthy that, even though the studied H_2O_2 concentration in their case was high (10 mM), their $^\bullet$OH generation rate was still slow in comparison with the results presented in this work. This again points out to the critical role of the GSH initial concentration: the presence of GSH is directly related with the generation rate of Fenton-active species. Wang et al.[61], found a higher peroxidase-like activity when Cu-hexacyanoferrate nanoparticles were pretreated with GSH. Also pH has a critical influence on Fen-

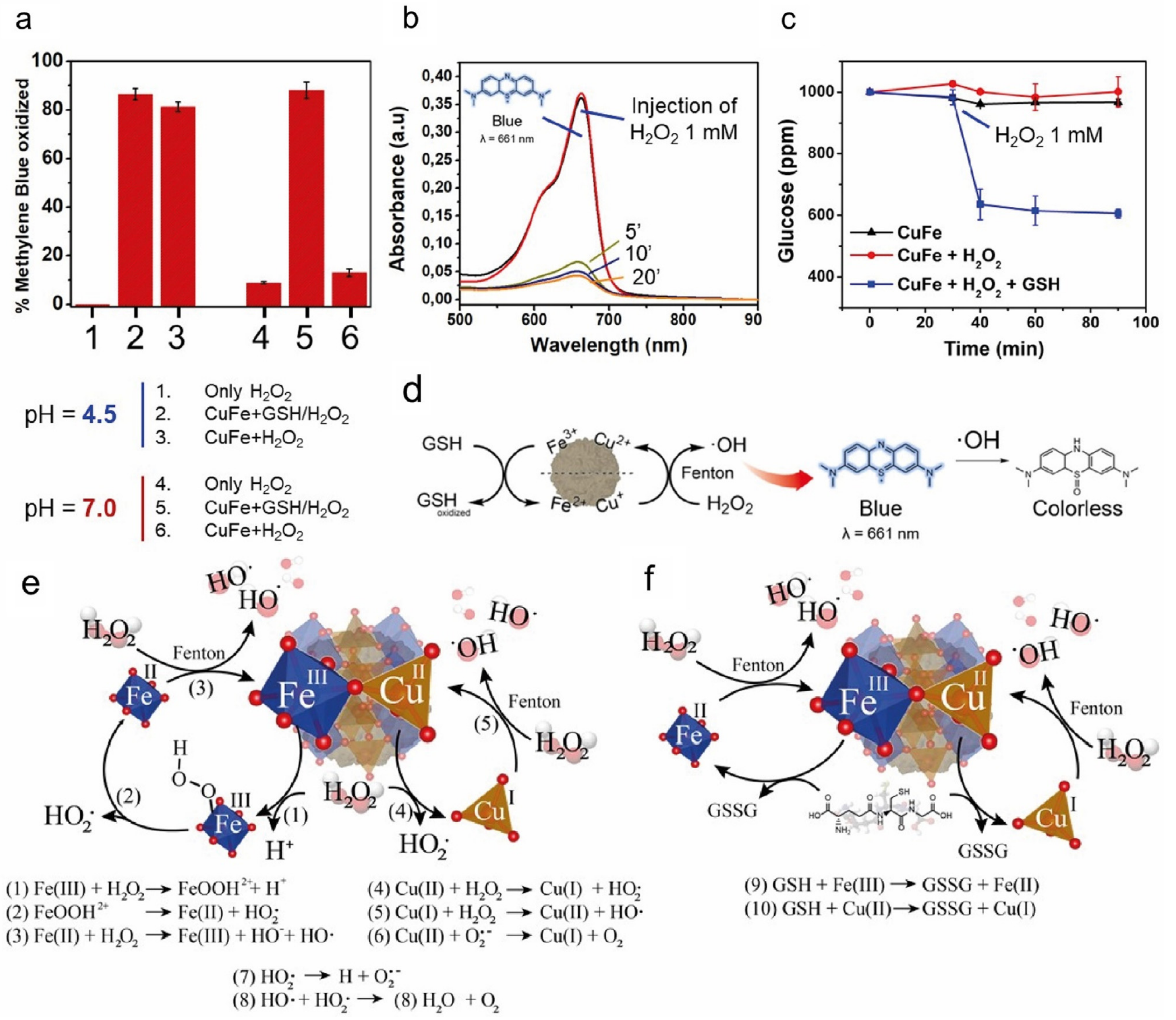

Fig. 4. CuFe assisted ·OH generation experiments. (a) Percentage of methylene blue oxidized after 20 min of reaction at pH = 4.5 (scenarios 1–3) and at pH = 7.0 (scenarios 4–6); (b) Evolution of MB over time under scenario 5 (CuFe + GSH/H_2O_2) at pH = 7.0, $[GSH]_0$ = 5 mM; (c) Glucose conversion under different reaction scenarios at pH7.0; d) Schematic representation of CuFe mechanism: after reaction with GSH, the generated Fe(II) and Cu(I) species can decompose H_2O_2 into ·OH which can be detected via MB reaction; Reaction conditions: [CuFe] = 0.1 mg·mL^{-1}, $[GSH]_0$ = 5 mM, $[H_2O_2]_0$ = 1 mM, $[MB]_0$ = 5.78·10^{-5} M. In 4c H_2O_2 was added to the system after 40 min of reaction. (e-f) Interaction between GSH and CuFe nanoparticles towards ·OH generation. (e) The generation of Fe(II) and Cu(I) active Fenton species through reactions (1,2) and (4), respectively, represents the bottleneck of the catalytic process. (f) The presence of GSH acts as an accelerator, providing the required reduction power to generate these active Fenton species through reactions (9) and (10).

ton reaction, since hydroxide ions (OH^-) can complex Fe and Cu centers of the catalyst [72]. Heterogeneous Fenton reaction starts after the interaction of H_2O_2 with the surface of the metal [41], being in several cases the Rate Determining Step (RDS) [73]. The higher the pH, the more complexed the CuFe surface by OH^- ions will be, thereby hindering the coordination of H_2O_2 and the subsequent formation of ·OH. A similar trend has been observed in homogeneous Fenton catalysis [40]. This may explain the result obtained for CuFe catalyst towards •OH production. At pH = 4.5, the large [H^+] is enough to drive the reaction following the mechanism presented in Fig. 4e where the H_2O_2 can act also as reducing agent, so the influence of GSH in the metal reduction is negligible. However, given the slower kinetics of Fenton reactions at pH = 7.4, the reduction power of GSH is critical to generate the active Fenton species following Fig. 4f.

We also analyzed the influence of GSH on metal leaching (Fig. S7): the presence of GSH quickly releases Cu from the crystalline structure. This is in contrast with the behaviour observed for iron, which only starts to be leached significantly once the preferential release of Cu has occurred to a large extent. An enhanced Cu leaching in the presence of GSH was also reported by Xu et al. with Cu-Mn based biodegradable nanoparticles [66] although in this case, Mn release also took place at the same time. They attributed the Cu-leaching to the high lability of Mn-O bond under tumor-microenvironment conditions (i.e. large GSH concentrations and mildly-acidic pH). The breakage of the Mn-O induced the formation of lattice defects [74] which led to the cleavage of Cu-O bonds.

The capacity of the same GSH-activated mechanism to target glucose, was also evaluated as this is a key molecule for cancer cell metabolism. The results are shown in Fig. 4c. It can be seen that, while there is little or no effect of the catalyst alone or with H_2O_2 added, when GSH is present a similar trend to that observed for MB follows, with a fast decrease of glucose concentration (up to

70% from 5.5 mM a value that could be considered representative of physiological concentrations) as soon as H_2O_2 (1 mM) was added when GSH was present in the system. From the above discussion we attribute this behavior to the generation of Fe(II) and Cu(I) active species on the catalyst mediated by GSH (reactions 9 and 10, Fig. 4f). Glucose is especially important in tumors and is being proposed as a central target of the so-called starvation therapy, focusing on glucose metabolism to hinder tumor growth [75].

Tumor cells consume an abnormally high amount of glucose in comparison with healthy ones to satisfy their energy needs and the anabolic demands for growth [10]. This glucose dependency has been known for a century and is generally known as the Warburg effect [76]. The strong depletion of glucose shown in Fig. 5c validates the potential of CuFe nanoparticles to generate ROS able to convert glucose as an attractive alternative to other catalysts exhibiting glucose oxidase-like activity [77].

2.4. Cellullar uptake and CuFe biocompatibility

The tolerability of exposure to CuFe NPs of cancer (U251-MG) and mesenchymal stem cells (hpMSCs) was determined by incubating increasing quantities of the catalyst with the respective cells during 6 and 24 h, respectively. According to the ISO 10993–5 (Biological evaluation of medical devices. Part 5: test for *in vitro* cytotoxicity) a reduction in cell viability higher than 30 % compared to the control is considered as cytotoxic effect. Fig. 5a and Fig. 5b show that a clear decrease on cell viability could be observed above a certain concentration of CuFe NPs. Interestingly, the vulnerability of U251-MG cancer cells to these nanoparticles was significantly higher compared to hpMSCs after incubation. Thus, after 6 h of incubation, 1.5 mg mL^{-1} and 0.4 mg mL^{-1} of CuFe were the doses that significantly reduced cell viability in hpMSCs and U251-MG cells (compared with untreated cells), respectively (i.e. hpMSCs can tolerate concentrations of CuFe NPs that are nearly four times the corresponding levels for U251-MG cells). Similar results were obtained also after a 24 h incubation period, with cell viability significantly affected at 0.4 and 0.1 mg mL $^{-1}$ for hpMSCs and U251-MG cells respectively, compared to untreated cells, again a factor of four. These data suggest that the viability of cancer glioma cells is more strongly affected upon the exposure to CuFe NPs compared with healthy hpMSC cells. To further study the interaction of these nanoparticles with both types of cells, a CuFe concentration of 0.1 mg mL^{-1} was selected as subcytotoxic dose lines in the subsequent experiments. The internalization of CuFe into U251-MG cells and hpMSCs was assessed by confocal microscopy. Fig. 5c and Fig. 5d (and Fig. S8) include representative images from hpMSCs and U251-MG cells, respectively, after treatment with CuFe for 4, 6, 10, 24 and 48 h. After 6 h a significant accumulation of CuFe inside both cell lines was observed, higher than at other time points studied. The internalization route was studied by marking lysosomes and CD63 positive endosomes and investigating their co-localization with CuFe NPs under confocal microscopy. The results (see the Z-stack sections of the images in Fig. 5 as well as in Figures S8 and S9) confirmed the localization of the CuFe NPs within an endosomal pathway, with preference to the lysosomal route. This is a favorable result, as a faster CuFe degradation would take place in the lysosomal acidic compartments within the cells.

2.5. Estimation of intracellular GSH concentration

Encouraged by the above findings on the role played by GSH in enhancing the catalytic effects of CuFe NPs, we decided to investigate whether the higher sensitivity exhibited by U251-MG cells could be related to their GSH content. Although it is generally known that cancer cells tend to increase the production of GSH compared with healthy cells, (a feature that is thought to be related to the role of GSH as antioxidant molecule) [19], to date there are no systematic studies correlating catalytic effects to GSH levels which is likely due to the lack of an accurate method to determine intracellular GSH levels. Here, we estimated the cytoplasmic GSH concentration in U251-MG and hpMSCs by: i) measuring GSH levels in cells after their tryptinization, lysate and derivatization with DTNB for a subsequent quantification using UPLC-PDA (see Fig. 6a and Experimental section) and ii) relating the amount of GSH determined to the number of cells present in the sample and to the cell volume (to estimate GSH concentrations

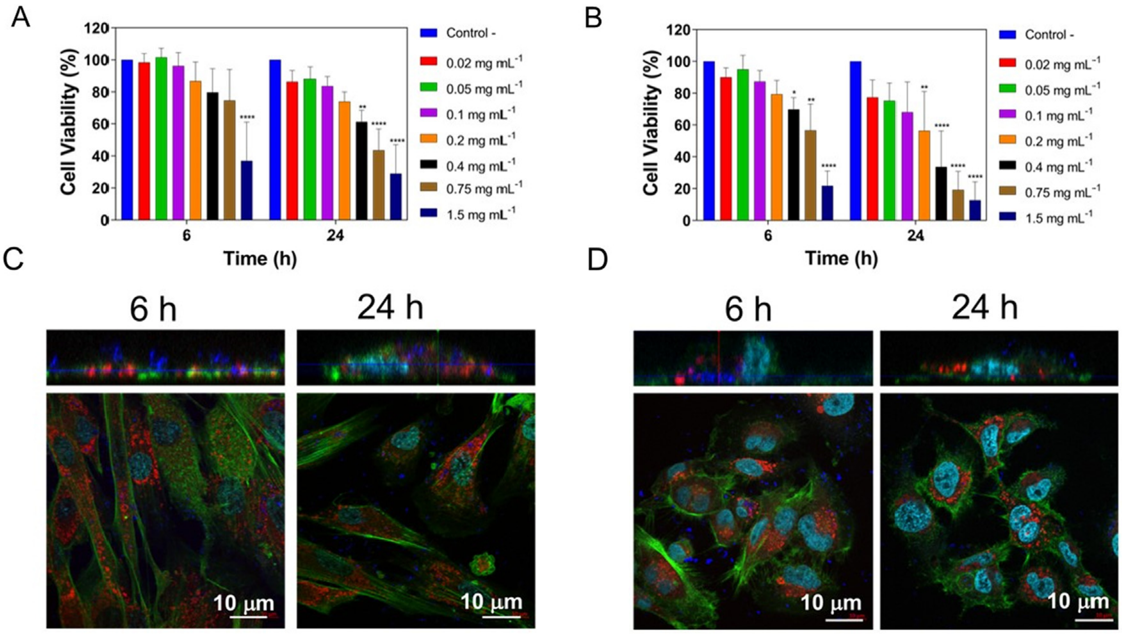

Fig. 5. (a) Tolerability study of CuFe incubated with hpMSCs cells after 6 h and 24 h. (b) Tolerability study of CuFe incubated with cancer U251-MG cells after 6 and 24 h (n = 4). (c) Confocal trafficking study of CuFe in hpMSCs showing endosomal pathway. (d) Confocal trafficking study of CuFe in U251-MG cells showing endosomal pathway (actin is shown in green, nuclei in cyan, CuFe in blue and CD63 positive vesicles in red).

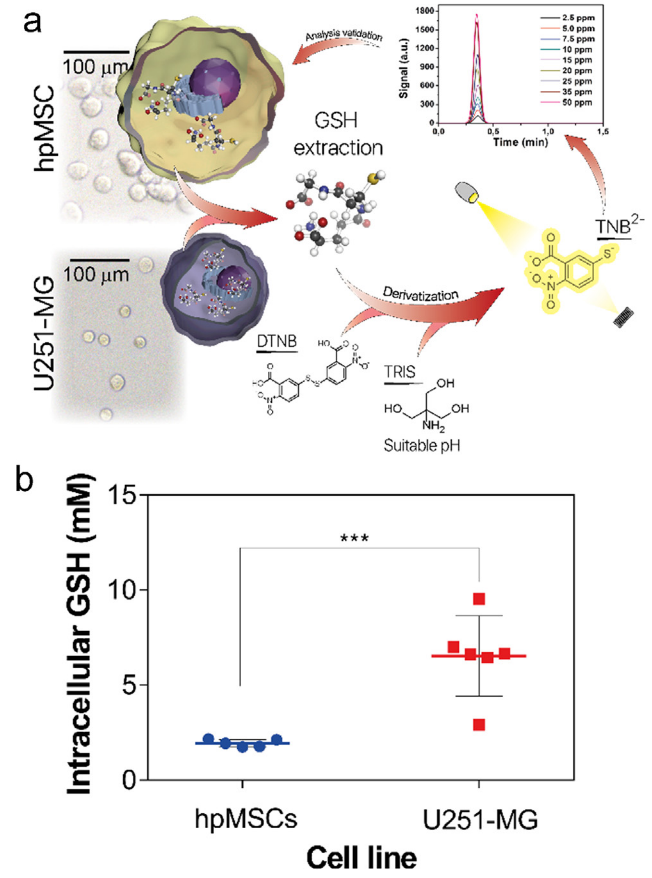

Fig. 6. Scheme summarizing the intracellular GSH quantification method developed in this work: (a) GSH extraction from cells after trypsinization, lysate and derivatization with DTNB for final quantification by UPLC-PDA analysis. GSH intracellular concentrations were expressed on a cell volumetric basis taking into account number of cells in the culture and their volume, obtained from optical inverted microscopy images; (b) Intracellular GSH concentration for hpMSCs and U251-MG lines, evidencing the larger amount of GSH in the latter (n = 6).

inside each individual cell) (Fig. 6a). Cell volumes were estimated from optical images obtained from cells in suspension with an inverted optical microscope (Olympus IX81) (Fig. 6a and Fig. S10b). As expected, the suspended cells had an approximately spherical morphology and their average radius were calculated as 14.4 ± 4.6 μm and 9.2 ± 1.8 μm for hpMSCs and U251-MG cells, respectively (Fig. S10a). According to these mean values, hpMSCs and U251-MG cells presented a total volume of 1.2×10^{-11} L and 3.3×10^{-12} L per cell, respectively. Then, the total amount of GSH determined by UPLC on the cell culture could be related to the total cell volume, taking into account the volumes of each cell and the number of cells in the respective cultures. Fig. 6b shows intracellular GSH levels estimated for both types of cells and it can be seen that in the case of U251-MG cancer cells GSH concentrations were significantly higher 7.3 ± 1.2 mM compared to 1.9 ± 0.2 mM for hpMSCs cells.

2.6. Cell death mediated by CuFe nanoparticles

The ability of CuFe nanocatalyst to induce cell death through by Fenton-type reactions was evaluated in both cancer and stem cells. Specifically, the cell cycle distribution and death mechanisms were studied by flow cytometry. Fig. 7 shows that, when exposed to CuFe NPs (0.2 mg·mL^{-1}) both cell lines undergo changes in the distribution of cells in each cycle phase, but a clearly more acute effect was observed on U251-MG cells leading to cell death (Fig. 7a). In fact, in some cases it was not even possible to evaluate the distribution of cells in each phase of the cell cycle because tumoral cells were strongly affected by CuFe particles (Fig. 7a). A significant increase in S phase (from 1.8 to 30.6 %) as well as in G2-M phase (<10%) and a decrease on G0-G1 phases (almost a 40 % decrease) was observed after cancer cell treatment compared to control samples (Fig. 7b and Table S4). Flow cytometry also elucidated the mechanism of cell death caused by CuFe (Fig. 7c). The incubation of the two cell lines (hpMSCs and U251-MG cells) with 0.2 mg mL^{-1} of CuFe during 6 and 24 h did not exhibit remarkable changes compared to control (untreated) samples regarding the percentage of cells death by necrosis. However, after CuFe NPs treatment, apoptosis was induced for both cell lines, again much more intensely for U251-MG cells (see Fig. 7d). Thus, for hpMSCs, 16.7 and 46.5% of cells were in a late apoptotic phase after 6 and 24 h of incubation with CuFe, respectively while in the case of cancer U251-MG cells the corresponding percentages were 34.3 % and 72.6 % respectively when they were incubated with the same concentration of CuFe nanoparticles at 6 and 24 h, respectively. Especially in late apoptosis, very significant increases were observed for U251-MG cells. Finally, the evolution of cell morphology by confocal microscopy also corroborates the results of flow cytometry regarding the effect of CuFe nanoparticles. Fig. 8a shows how U251-MG morphology was strongly affected upon CuFe treatment (particularly after 24 h of incubation). The presence of the nanocatalyst caused the features typical of apoptosis including spherical rounded shape, cytoplasmatic aggregation, membrane irregularity and the formation of multiple apoptotic bodies compared with untreated cells. Interestingly, apoptosis features are not yet evident the microscopy images of hpMSCs incubated with CuFe NPs under the same conditions, even though CuFeNPs are clearly present inside MSC cells. These data again confirm the enhanced effect of CuFe nanocatalyst in the cancer cells studied compared to the stem cell counterparts.

GSH levels inside both hpMSCs and U251-MG cells after their treatment with CuFe were measured. U251-MG cells exhibited a very significant decrease on GSH intracellular levels when treated with CuFe compared to control cells (untreated) (see Fig. 8b). Specifically, the presence of the nanocatalyst led to an abrupt decrease of cytoplasmatic GSH from 7.3 mM to 5.2 mM (6 h) and to 2.5 mM (24 h) in the cancer cells. These results demonstrate an enhanced cytotoxic response towards the U251-MG tumor cell line, being much more susceptible to GSH depletion compared to stem cells after their interaction to CuFe NPs. Taking together, the results of flow cytometry and confocal microscopy indicate that: i) after CuFe exposure, U251-MG cancer undergo intense apoptosis compared with hpMSCs, a catalytic action that is triggered by the high GSH levels inside U-251-MG cells; and ii) U251-MG GSH levels significantly decrease when incubated with CuFe compared to hpMSCs (Fig. 7b) as a result of the above-described cascade processes.

3. Experimental section

3.1. Chemicals and materials

Iron (III) chloride hexahydrate ($FeCl_3 \cdot 6H_2O$, 97%), copper (II) chloride dihydrate ($CuCl_2 \cdot 2H_2O$, ≥ 99.0%), sodium acetate anhydrous (CH_3COONa), Bovine Serum Albumin (BSA), ethylene glycol (EG) (99.8%), Glutathione (≥98, HPLC), Glutathione oxidized (≥98, HPLC), 5,5′-Dithiobis(2-nitrobenzoic acid) (DNTB), lactose (Standard Quality), methylene blue (MB), hydrogen peroxide (H_2O_2, 33% v/v), sodium bicarbonate ($NaHCO_3$, 99%) were purchased from Sigma Aldrich. D-glucose was purchased from MP

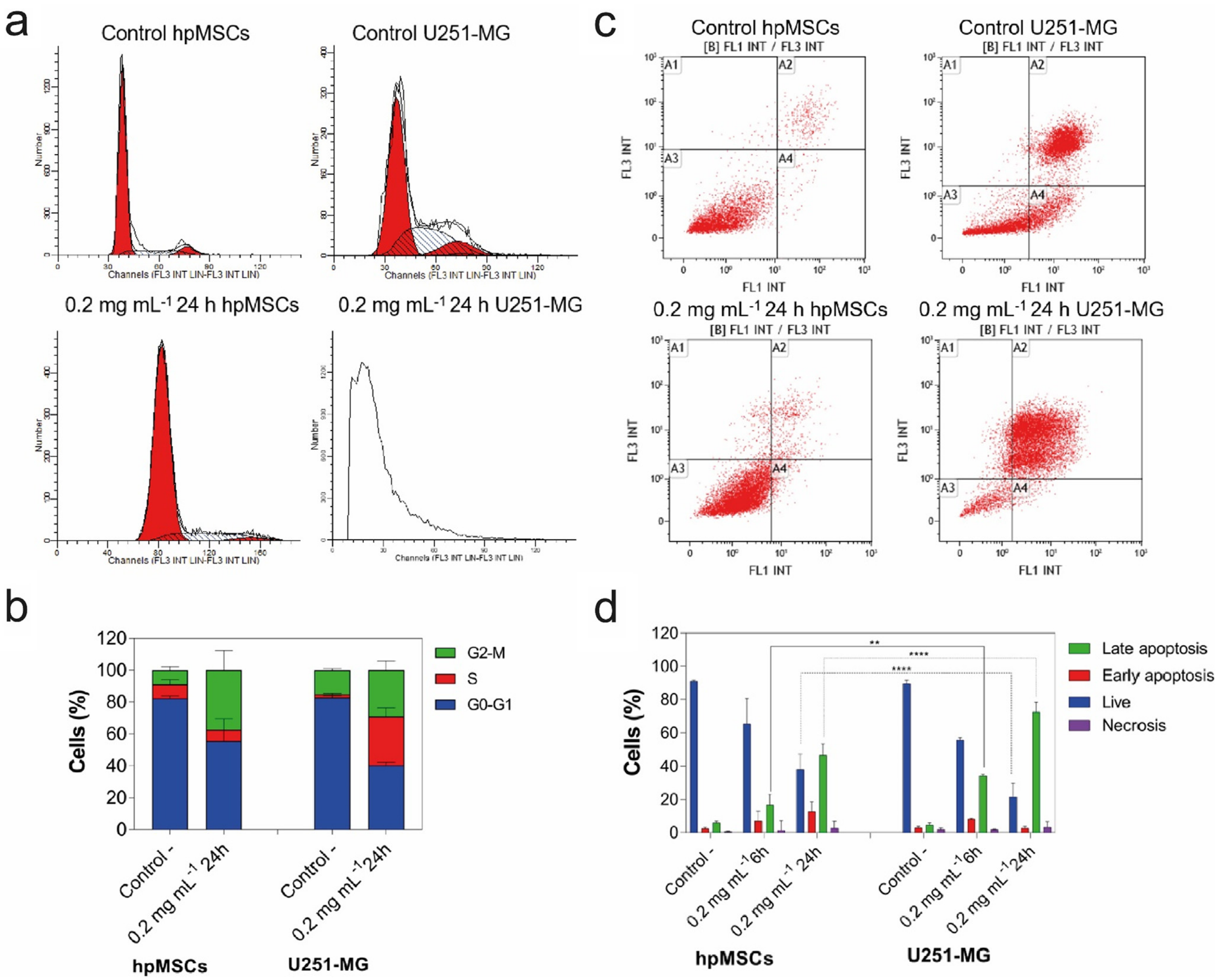

Fig. 7. Flow cytometry analyses: (a) Cell cycle histograms obtained by flow cytometry; (b) Percentage of cells in cell cycle after the treatment with CuFe during 24 h at 0.2 mg mL^{-1} compared to untreated cells (control); (c) Apoptosis and necrosis results obtained by flow cytometry; (d) Percentage of cells in early or late apoptosis and necrosis after the treatment with CuFe during 24 h at 0.2 mg mL^{-1} compared to untreated cells (control).

Biomedicals. Acetonitrile (ACN) (HPLC Quality) was purchased from WVR (Avantor) . UPLC grade water was obtained from a Milli-Q Advantage A10 System with resistivity of 18.2 mΩ (Merk Millipore, Germany).

3.2. Synthesis of CuFe nanoparticles

$CuFe_2O_4$ nanoparticles were synthetized following a templated-growth method. In a typical synthesis, 250 mg of BSA were dissolved in 2.5 mL of deionized water. After that, 12.5 mL of EG were added to the mixture, followed by 270.5 mg of $FeCl_3 \cdot 6H_2O$, 121.0 mg $CuCl_2 \cdot 2H_2O$ and 375 mg of CH_3COONa. Reagents were thoroughly stirred for 2 h at room temperature. The reaction was then transferred to a Teflon autoclave and the temperature was kept at 180 °C for 24 h. Finally, the product was centrifuged at 12 000 rpm for 20 min and washed twice in the same conditions with distilled water. The catalyst was stored at 4 °C until further use. The synthesis of these materials has been performed at the Platform of Production of Biomaterials and Nanoparticles of the NANBIOSIS ICTS, more specifically by the Nanoparticle Synthesis Unit of the CIBER in BioEngineering, Biomaterials & Nanomedicine (CIBER-BBN).

3.3. Characterization techniques

Transmission electron microscopy (TEM) was performed using a FEI TECNAI T20 microscope operated at 200 keV. Samples were prepared by dropcasting 5 μL of the nanoparticle suspension on a holey carbon TEM grid. High-resolution transmission electron microscopy (HRTEM) was performed using a FEI Titan (80–300 kV) microscope at an acceleration voltage of 300 kV. Sample was prepared by depositing 5 μL of the nanoparticle suspension on a holey carbon TEM grid. UV–vis spectra were obtained on a UV–vis double beam spectrophotometer Jasco V67. Fourier transform infrared spectroscopy (FTIR) was performed on a Bruker Vertex 70. X-ray photoelectron spectroscopy (XPS) was performed with an Axis Supra spectrometer (Kratos Tech). The samples were mounted on a sample rod placed in the pretreatment chamber of the spectrometer and then evacuated at room temperature. The spectra were excited by a monochromatized Al Kα source at 1486.6 eV and subsequently run at 8 kV and 15 mA. A survey spectrum was measured at 160 eV of pass energy, and for the individual peak regions, spectra were recorded with a pass energy of 20 eV. Analysis of the peaks was performed with the CasaXPS software using a weighted sum of Lorentzian and Gaussian component

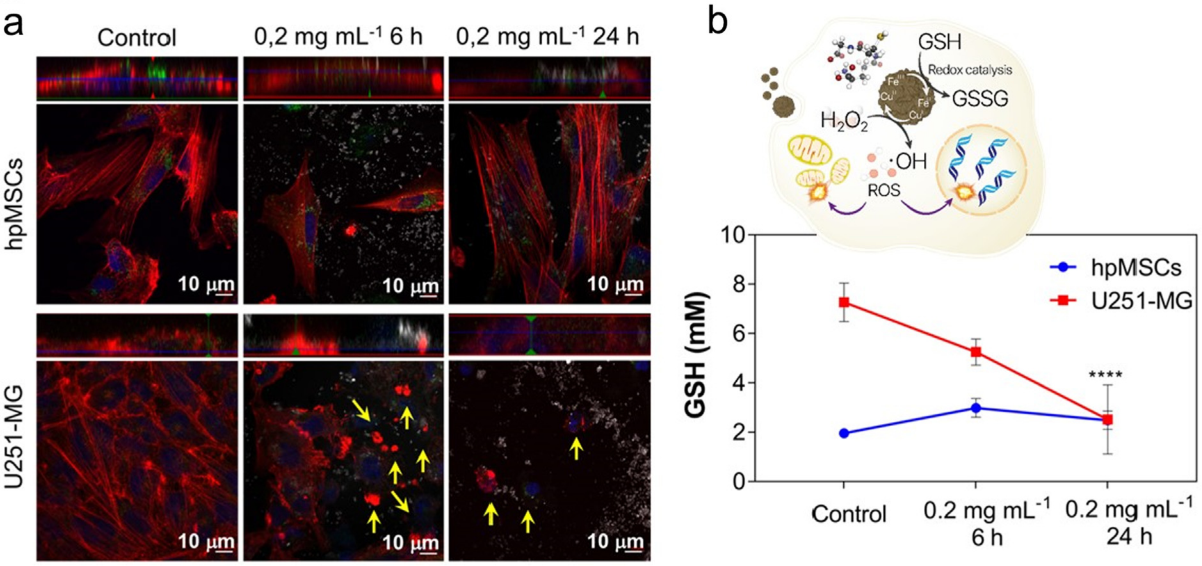

Fig. 8. (a) Morphological changes of cells incubated with CuFe during 6 and 24 h (0.2 mg mL^{-1}). Actin is visualized in red, CD63 positive vesicles in green, nuclei in blue and CuFe in white; (b). Evolution of intracellular GSH levels of hpMSCs and U251-MG after their incubation with the nanocatalyst or under control (non-treated) conditions. Inset illustrates the GSH depletion-ROS generation cycle (n = 3).

curves after Shirley background subtraction. The binding energies were referenced to the internal C 1 s standard at 284.5 eV. X-ray diffraction patterns were obtained in a PANalytical Empyrean equipment in Bragg-Brentano configuration using CuKα radiation and equipped with a PIXcel1D detector. ^{1}H spectra (D_2O) were recorded at 25 °C using a Bruker Avance 400 MHz NMR spectrometer with TMS as the internal standard and deuterated water as solvent in a 5 mm QNP probe. Nanoparticle Tracking Analysis was measured on Malvern Nanosight 300.

3.4. Catalytic oxidation of GSH

The catalytic activity of $CuFe_2O_4$ nanoparticles oxidizing GSH was evaluated according to the following protocol: in a total volume of 2.5 mL, 5 mM of GSH were mixed with 0.1 mg·mL^{-1} of CuFe at 37 °C. In the experiments adding H_2O_2, the final concentration in the reaction was fixed at 0.5 mM. GSH concentration was quantified by UPLC (vide infra).

3.5. Generation of hydroxyl radicals

The capability of CuFe nanoparticles to generate ·OH was evaluated via MB assay [29,66]. In a total volume of 2.5 mL, a final concentration of $5.78 \cdot 10^{-5}$ M of MB and 0.1 mg·mL^{-1} of CuFe were mixed. For experiments containing GSH, a concentration of 5 mM was selected. The pH of the reactions was set to 4.5 and 7.0 using CH_3COO/CH_3COOH and PBS buffer, respectively. H_2O_2 was added after 40 min with a final concentration of 1 mM. Alternatively, ·OH formation was detected via the terephtalic acid assay [60,78,79]. In a total volume of 2.5 mL, 5 mM of disodium terephthalate, 0.1 mg·mL^{-1} CuFe and 5 mM of GSH were mixed. The pH was maintained at 4.5 using a CH_3COO^-/CH_3COOH buffer. H_2O_2 was added after 25 min of reaction, with a final concentration of 1 mM. The generation of 2-hydroxy disodium terephthalate was evaluated by measuring the fluorescence with an excitation wavelength of 315 nm.

3.6. Cell culture conditions

hpMSCs were obtained from Cellular Engineering Technologies (CET) (Coralville, IA, USA) and U251-MG glioblastoma cells were kindly obtained from Cancer Research UK Cell services. hpMSCs were cultured in Dulbecco's modified Eagle's medium (DMEM; Biowest, France) supplemented with 5 g mL^{-1} of FGF-2 growth factor (PeproTech, USA), with 10 % of fetal bovine serum (FBS, GIBCO, USA), 1% penicillin/streptomycin and 1% amphotericin (Biowest, France) and maintained at 37 °C in a 5% CO_2-humidified atmosphere under hypoxic conditions (3 %). For culturing U251-MG cells DMEM with 10 % of FBS supplemented with 1% penicillin/streptomycin and 1% amphotericin was used.

3.7. Study of CuFe nanoparticles biocompatibility

hpMSCs and U251-MG cells were seeded in a 96-well plate format (at 5000 and 4000 U251-MG cells and hpMSCs per well, respectively) and incubated for 24 h before treatment. Each well was then replaced with a suspension of CuFe in culture media at a concentration ranged from 0.025 to 1.5 mg mL^{-1} After 6 and 24 h cells were washed with PBS buffer. Blue Cell viability reagent (10% v/v) was used to determine cell viability under the effect of CuFe [80]. Experiments were performed in triplicates.

3.8. Cellular uptake and trafficking of CuFe nanoparticles

Confocal microscopy was employed to follow the internalization of CuFe in both hpMSCs and U251-MG cells. hpMSCs and U251-MG cells were seeded at a density of 30,000 and 20,000 U251-MG cells and hpMSCs per well, respectively onto 20 mm cover slips (deposited onto a 24-well plate) and incubated under standard culture conditions for 24 h. Then, CuFe at the subcytotoxic dose (0.1 mg·mL^{-1}) were added to each well and incubated for 4, 6, 10, 24 and 48 h. Cells were finally fixed with 4 % paraformaldehyde. In order to label the cytoplasmic actin, cells were stained with phalloidin-Alexa546 (Invitrogen, USA), the endosomal pathway was labelled using an anti-CD63-Alexa-488 (ThermoFisher Scientific) and Draq-5 was used to observe the nuclei. Reflection of the incident light at 488/490 nm was used to directly visualize CuFe aggregates. Lysosomes were also labelled using a Lysotracker Green DND-26 (molecular probes) without previously fixing the cells and following manufacturer instructions. The cellular uptake was observed under a confocal microscope (SEISS LSM880 Confocal Laser Scanning Microscope) with a 63x oil immersed N.A. 1.40 objective. Z-stack orthogonal projections were developed to determine the presence of NPs inside the cytosol.

3.9. Intracellular GSH quantification

In order to determine the intracellular GSH concentration, U251-MG and hpMSCs were seeded onto P100 culture dishes upon they reach 80 % of confluence. Cells were finally trypsinized, washed twice with PBS (500 g, 5 min) and collected. Before GSH quantification, cells were centrifuged twice at 13300 rpm for 5 min. Supernatant was discarded and a certain volume of 12% CCl_3COOH solution was added to lysate the cells and precipitate proteins avoiding its interference in the analysis (500 μL for GSH determination and 400 μL for GSH-consumption experiments). Samples were sonicated and left 15 min at 4C. The suspension was centrifuged at 13 300 rpm for 5 min. The supernatant was isolated for derivatization process (see details below) and labelled as *in vitro*. In order to express the result in terms of GSH cell concentration, an estimation of total cell volume in the samples was established. After quantifying the number of cells in each sample, and assuming 3-dimensional spherical shapes, average cell volumetric distribution was estimated after measuring the radius of 250 individual cells from inverted conventional microscopy images (see Fig. S10b). Average radii of 14.4 ± 4.6 mm and 9.2 ± 1.8 mm were determined for hpMSCs and U251-MG cells, respectively), Likewise, hpMSCs presented a calculated volume of 1.2×10^{-11} L whereas U251-MG volumes were 3.3×10^{-12} L.

3.10. GSH derivatization protocols for UPLC analysis

The derivatization of GSH using DTNB yields a quantifiable yellow-colored product, 5-thiobis-(2-nitrobenzoic acid) (TNB^{2-}) which absorbs at 412 nm following reaction shown in Fig. S3. Depending on the experiment (ex vitro GSH oxidation or *in vitro* GSH quantification), analysis conditions are different due to matrix differences. In the case of catalytic oxidation of GSH, a calibration curve was prepared following the amounts specified in Table S2. For the sample preparation, 20 μL of the reaction were mixed with 100 μL of 1 mM DTNB, 50 μL of 0.2 M $NaHCO_3$ and 880 μL of ACN: H_2O (1:1) solutions. For *in vitro* GSH quantification, calibration curve was prepared following the amounts specified in Table S3. Due to the acidic nature of TCA employed for GSH extraction, during the sample preparation, 50 μL of *in vitro* GSH solution were mixed with 20 μL DNTB (2.5 mM), 6.5 μL NaOH (3 M) and 930 μL TRIS (0.01 M) solution. Final pH both of standards and samples was 7.8–7.9. Both samples and standards were filtered with 0.22 μm Nylon filters before injecting in UPLC system.

3.11. UPLC-PDA-MS equipment for GSH and glucose analysis

GSH and glucose analysis were performed on Waters ACQUITY system H-Class which consisted of a binary pump, an autosampler, a column thermostat and a photodiode array (PDA) detector. This system is coupled to a single quadrupole mass spectrometer with an electrospray ionization (ESI) ACQUITY QDa mass detector. Data acquisition and processing were performed by using MASSLYNX software (Waters Corporation USA). On the one hand, in order to analyze GSH from derivatized samples as describe below, chromatographic separation was performed using an ACQUITY UPLC BEH C18 column (130 Å, 1.7 μm 2.1 × 50 mm, from WATERS) at 40 °C under an isocratic flow of 0.3 mL/min containing 50% acetonitrile, 50% milli Q water. PDA detector was employed to monitor absorbance from derivatized GSH at 412 nm during analysis time.

On the other hand, glucose was monitored after the chromatographic separation was performed using an ACQUITY UPLC BEH Amide column (130 Å, 1.7 μm, 2.1 mm X 100 mm, WATERS). In this case, mobile phase consisted of an initial mixture of acetonitrile/water (90:10), containing 0.1% 10 mM ammonium chloride in ammonium, as a mobile phase modifier, at a 0.5 mL/min initial flow rate. Thereon a gradient in the mobile phase was employed to separate the different metabolites present in the samples. Water composition increased for 3 min until a 65% acetonitrile is reached and then the system can recover initial conditions. ACQUITY QDa mass detector was employed to quantify sugar concentrations according to the most abundant ions generated as described below. Calibrations were performed using commercial standards of glucose and lactose.

3.12. Cell viability and intracellular GSH levels depletion

To determine how CuFe presence within cell cytoplasm leads to cell death mediated by GSH decrease, firstly the distribution of the cell cycle phases after CuFe treatment was assessed by flow cytometry. Cells were seeded onto 6-well plates at a density of 200,000 and 300,000 hpMSCs and U251-MG cells per well, respectively. After 24 h, CuFe (0.2 mg mL^{-1}) were added into the treated wells. After 24 h, cells were trypsinized and washed twice with PBS (500 g, 5 min). Then, cells were collected in PBS and fixed with 70 % ice-cold ethanol and maintained at 4 °C in this solution almost for 24 h. DNA staining was performed by adding RNase A and propidium iodide (PI) to the cell suspension. Finally, samples were analyzed in a FACSARRAY BD equipment with the MODIFIT 3.0 Verity software. Control samples (not treated cells) were also evaluated to estimate the standard distribution of cell cycles in the cell lines assayed. Moreover, cell morphology was evaluated upon their exposure to CuFe 0.2 mg mL^{-1} during 6 and 24 h by confocal microscopy as previously mentioned.

In order to study cell mechanisms induced by the presence of CuFe, cells were again seeded onto 6-well plates and CuFe was added at previously mentioned (0.2 mg mL^{-1} during 6 and 24 h). After these time points, cells were collected and washed twice with PBS. Cell pellet was finally suspended in 200 μL of PBS containing ethylenediaminetetraacetic acid (EDTA) before cell labeling with 5 μL of Anexin V-FITC and 5 μL of PI during 15 min. Cancer cell mechanism (necrosis or apoptosis) was determined by flow cytometry (FACSAria BD cytometer, BD Bioscience). Flow cytometry experiments were performed in triplicates. Finally, GSH intracellular levels of CuFe treated hpMSCs or U251-MG cells (0.2 mg mL^{-1} during 6 and 24 h) were quantified as described above in order to corroborate that CuFe lead cytotoxicity effect is mediated by GSH depletion inside cell cytoplasm. Experiments were performed in triplicates.

3.13. GSH triggered conversion of glucose

GSH-assisted peroxidation of glucose was carried out as follows: 1000 ppm of glucose (5.55 mM) were mixed with 0.05 $mg \cdot mL^{-1}$ of CuFe at 37 °C in a total volume of 2.5 mL. For experiments containing GSH, a concentration of 5 mM was established. 100 μL H_2O_2 (125 mM) were added after 30 min of reaction to reach a final concentration of 1 mM. The pH was adjusted to 7.0 with $NaHCO_3$ solution. Glucose concentration from samples collected at different times were analyzed by UPLC-MS. After ESI, glucose most abundant ion is the chloride adduct [M−Cl-] at *m/z* formed due to the presence of NH_4Cl in the mobile phase [81]. Calibration curve was prepared following the amounts specified in

Table S6. Lactose was used as internal standard, being 377.45 the m/s corresponding to its most abundant chloride adduct. For the sample preparation, 20 μL of reaction was mixed with 25 μL of 1000 ppm Lactose solution and 955 μL of a mixture ACN:H_2O (1:1). Both samples and standards were filtered with 0.22 μm Nylon filters before injecting in UPLC system.

3.14. Statistical analysis

All the results are expressed as mean ± SD. Statistical analysis of the biological experiments and the significant differences among the means were evaluated by two-way analysis of variance (ANOVA) for multiple comparisons by Dunnett's multiple comparisons test using GraphPad Software). Statistically significant differences were express as follows: *$p < 0.05$, **$p < 0.005$, ***$p < 0.0005$ and ****$p < 0.00005$.

4. Conclusions

The CuFe nanoparticles synthesized in this work can enable a GSH-triggered cascade reaction that gives rise to the depletion of intracellular GSH in a process that produces reduced species on the surface of the nanoparticles. These reduced species in turn promote Fenton processes in the presence of H_2O_2 and the subsequent generation of ROS species that induce cell death by apoptosis. Especially at close to neutral pH, the catalytic action needs the presence of both GSH and H_2O_2 as a trigger, and is strongly enhanced by higher GSH concentrations. Our comparative study with hpMSCs and U251-MG cells as examples of healthy and cancer cells support this conclusion: CuFe nanoparticles were much more toxic towards U251-MG cells leading to an enhancement of apoptosis, as confirmed by flow cytometry and confocal microscopy observations. The effect was damped on hpMSCs, with considerably lower GSH basal levels. Both intra- and extracellular GSH levels were accurately measured in this work, and the concentrations correlated well with the catalytic action observed. Interestingly, the presence of GSH not only pulled the catalytic action regarding the reduction of GSH levels and the concomitant generation of ROS, but also the depletion of other molecules. Glucose in particular was tested in this work, undergoing a strong reduction in the presence of GSH, H_2O_2 and CuFe nanoparticles. In summary, the higher concentration of GSH in cancer cells enables a combined therapeutic action (ROS generation and starvation therapy through glucose depletion), leading to enhanced apoptosis. This could open up new opportunities that leverage GSH upregulation in the tumor environment, adding a new element to the growing chemodynamic therapy toolbox.

CRediT authorship contribution statement

Javier Bonet-Aleta: Conceptualization, Methodology, Validation, Formal analysis, Data curation, Writing – original draft, Writing – review & editing. **Maria Sancho-Albero:** Conceptualization, Methodology, Formal analysis, Validation, Data curation, Writing – original draft, Writing – review & editing. **Javier Calzada-Funes:** Methodology, Investigation, Validation, Data curation, Formal analysis, Writing – review & editing. **Silvia Irusta:** Validation, Data curation, Formal analysis. **Pilar Martin-Duque:** Methodology, Validation, Resources, Supervision, Writing – review & editing. **Jose L. Hueso:** Conceptualization, Methodology, Validation, Formal analysis, Supervision, Visualization, Writing – original draft, Writing – review & editing. **Jesus Santamaria:** Conceptualization, Supervision, Writing – original draft, Writing – review & editing, Resources, Visualization, Supervision.

Declaration of Competing Interest

The authors declare that they have no known competing financial interests or personal relationships that could have appeared to influence the work reported in this paper.

Acknowledgements

Financial support from the European Research Council (ERC-Advanced Grant CADENCE number 742684) is gratefully acknowledged. The TEM measurements were conducted at the Laboratorio de Microscopias Avanzadas, Instituto de Nanociencia de Aragon, Universidad de Zaragoza, Spain. The synthesis of materials has been performed by the Platform of Production of Biomaterials and Nanoparticles of the NANBIOSIS ICTS, more specifically by the Nanoparticle Synthesis Unit of the CIBER in BioEngineering, Biomaterials & Nanomedicine (CIBER-BBN). J.B-A. acknowledges the Spanish Government for an FPU predoctoral contract. We would also like to thank to the Scientific Services of the Aragon Institute of Health Sciences (IACS), specifically to the Cell culture, Microscopy, and Citometry Services and their specialist and the ICTS ELECMI.

Appendix A. Supplementary material

Supplementary data to this article can be found online at https://doi.org/10.1016/j.jcis.2022.03.036.

References

[1] WHO, World Health Organization: Global Health Estimates 2020: Deaths by Cause, Age, Sex, by Country and by Region, 2000-2019, World Health Organization: Global Health Estimates 2020: Deaths by Cause, Age, Sex, by Country and by Region, 2000-2019, (2020).

[2] Z. Tang, P. Zhao, H. Wang, Y. Liu, W. Bu, Biomedicine Meets Fenton Chemistry, Chem. Rev. 121 (4) (2021) 1981–2019.

[3] I.S. Harris, G.M. DeNicola, The Complex Interplay between Antioxidants and ROS in Cancer, Trends Cell Biol. 30 (6) (2020) 440–451.

[4] Y. Liu, H. Liu, L.i. Wang, Y. Wang, C. Zhang, C. Wang, Y. Yan, J. Fan, G. Xu, Q. Zhang, Amplification of oxidative stress via intracellular ROS production and antioxidant consumption by two natural drug-encapsulated nanoagents for efficient anticancer therapy, Nanoscale Adv. 2 (9) (2020) 3872–3881.

[5] B. Yang, Y.u. Chen, J. Shi, Nanocatalytic Medicine, Adv. Mater. 31 (39) (2019) 1901778.

[6] X. Wang, X. Zhong, Z. Liu, L. Cheng, Recent progress of chemodynamic therapy-induced combination cancer therapy, Nano Today 35 (2020) 100946.

[7] L. Wang, M. Huo, Y.u. Chen, J. Shi, Tumor Microenvironment-Enabled Nanotherapy, Adv. Healthcare Mater. 7 (8) (2018) 1701156, https://doi.org/10.1002/adhm.v7.810.1002/adhm.201701156.

[8] R.H. Burdon, Superoxide and hydrogen peroxide in relation to mammalian cell proliferation, Free Radical Biol. Med. 18 (1995) 775–794.

[9] M. López-Lázaro, Dual role of hydrogen peroxide in cancer: possible relevance to cancer chemoprevention and therapy, Cancer Lett. 252 (2007) 1–8.

[10] R.J. DeBerardinis, N.S. Chandel, Fundamentals of cancer metabolism, Sci. Adv. 2 (5) (2016), https://doi.org/10.1126/sciadv.1600200.

[11] B. Yang, Y.u. Chen, J. Shi, Reactive Oxygen Species (ROS)-Based Nanomedicine, Chem. Rev. 119 (8) (2019) 4881–4985.

[12] S.-L. Li, P. Jiang, F.-L. Jiang, Y.i. Liu, Recent Advances in Nanomaterial-Based Nanoplatforms for Chemodynamic Cancer Therapy, Adv. Funct. Mater. 31 (22) (2021) 2100243.

[13] Y. Xiong, C. Xiao, Z. Li, X. Yang, Engineering nanomedicine for glutathione depletion-augmented cancer therapy, Chem. Soc. Rev. 50 (10) (2021) 6013–6041.

[14] C. Maksoudian, N. Saffarzadeh, E. Hesemans, N. Dekoning, K. Buttiens, S.J. Soenen, Role of inorganic nanoparticle degradation in cancer therapy, Nanoscale Adv. 2 (9) (2020) 3734–3763.

[15] X. Lu, S. Gao, H. Lin, L. Yu, Y. Han, P. Zhu, W. Bao, H. Yao, Y. Chen, J. Shi, Bioinspired Copper Single-Atom Catalysts for Tumor Parallel Catalytic Therapy, Adv. Mater. 32 (2020) 2002246.

[16] C. Zhang, W. Bu, D. Ni, S. Zhang, Q. Li, Z. Yao, J. Zhang, H. Yao, Z. Wang, J. Shi, Synthesis of Iron Nanometallic Glasses and Their Application in Cancer Therapy by a Localized Fenton Reaction, Angewandte Chemie (International ed. in English), 55 (2016) 2101–2106.

[17] C. Liu, D. Wang, S. Zhang, Y. Cheng, F. Yang, Y. Xing, T. Xu, H. Dong, X. Zhang, Biodegradable Biomimic Copper/Manganese Silicate Nanospheres for

Chemodynamic/Photodynamic Synergistic Therapy with Simultaneous Glutathione Depletion and Hypoxia Relief, ACS Nano 13 (2019) 4267–4277.
[18] T.P. Szatrowski, C.F. Nathan, Production of Large Amounts of Hydrogen Peroxide by Human Tumor Cells, Cancer Res. 51 (1991) 794.
[19] A. Bansal, M.C. Simon, Glutathione metabolism in cancer progression and treatment resistance, J. Cell Biol. 217 (2018) 2291–2298.
[20] M.P. Gamcsik, M.S. Kasibhatla, S.D. Teeter, O.M. Colvin, Glutathione levels in human tumors, Biomarkers 17 (2012) 671–691.
[21] A.L. Ortega, S. Mena, J.M. Estrela, Glutathione in Cancer Cell Death, Cancers 3 (1) (2011) 1285–1310.
[22] H.J. Forman, H. Zhang, A. Rinna, Glutathione: overview of its protective roles, measurement, and biosynthesis, Mol. Aspects Med. 30 (2009) 1–12.
[23] S.C. Lu, Regulation of glutathione synthesis, Mol. Aspects Med. 30 (2009) 42–59.
[24] N.S. Kosower, E.M. Kosower, The glutathione status of cells, Int. Rev. Cytol. 54 (1978) 109–160.
[25] J.M. Estrela, A. Ortega, E. Obrador, Glutathione in Cancer Biology and Therapy, Crit. Rev. Clin. Lab. Sci. 43 (2006) 143–181.
[26] L. Kennedy, J.K. Sandhu, M.E. Harper, M. Cuperlovic-Culf, Role of Glutathione in Cancer: From Mechanisms to Therapies, Biomolecules 10 (2020).
[27] Y. Ding, Y. Dai, M. Wu, L. Li, Glutathione-Mediated Nanomedicines for Cancer Diagnosis and Therapy, Chem. Eng. J. 426 (2021) 128880, https://doi.org/10.1016/j.cej.2021.128880.
[28] Y. Liu, W. Zhen, L. Jin, S. Zhang, G. Sun, T. Zhang, X. Xu, S. Song, Y. Wang, J. Liu, H. Zhang, All-in-One Theranostic Nanoagent with Enhanced Reactive Oxygen Species Generation and Modulating Tumor Microenvironment Ability for Effective Tumor Eradication, ACS Nano 12 (2018) 4886–4893.
[29] L.-S. Lin, J. Song, L. Song, K. Ke, Y. Liu, Z. Zhou, Z. Shen, J. Li, Z. Yang, W. Tang, G. Niu, H.-H. Yang, X. Chen, Simultaneous Fenton-like Ion Delivery and Glutathione Depletion by MnO2-Based Nanoagent to Enhance Chemodynamic Therapy, Angew. Chem. Int. Ed. 57 (2018) 4902–4906.
[30] R. Franco, J.A. Cidlowski, Apoptosis and glutathione: beyond an antioxidant, Cell Death Differ. 16 (10) (2009) 1303–1314.
[31] M. Cox, D. Nelson, Lehninger Principles of Biochemistry, 2000.
[32] K.P. Bhabak, G. Mugesh, Functional Mimics of Glutathione Peroxidase: Bioinspired Synthetic Antioxidants, Acc. Chem. Res. 43 (11) (2010) 1408–1419.
[33] J. Liu, M. Wu, Y. Pan, Y. Duan, Z. Dong, Y. Chao, Z. Liu, B. Liu, Biodegradable Nanoscale Coordination Polymers for Targeted Tumor Combination Therapy with Oxidative Stress Amplification, Adv. Funct. Mater. 30 (2020) 1908865.
[34] S.-Y. Yin, G. Song, Y. Yang, Y. Zhao, P. Wang, L.-M. Zhu, X. Yin, X.-B. Zhang, Persistent Regulation of Tumor Microenvironment via Circulating Catalysis of MnFe2O4@Metal–Organic Frameworks for Enhanced Photodynamic Therapy, Adv. Funct. Mater. 29 (2019) 1901417.
[35] B. Ma, S. Wang, F. Liu, S. Zhang, J. Duan, Z. Li, Y. Kong, Y. Sang, H. Liu, W. Bu, L. Li, Self-Assembled Copper-Amino Acid Nanoparticles for in Situ Glutathione "AND" H2O2 Sequentially Triggered Chemodynamic Therapy, J. Am. Chem. Soc. 141 (2019) 849–857.
[36] M. Chang, M. Wang, M. Wang, M. Shu, B. Ding, C. Li, M. Pang, S. Cui, Z. Hou, J. Lin, A Multifunctional Cascade Bioreactor Based on Hollow-Structured Cu2MoS4 for Synergetic Cancer Chemo-Dynamic Therapy/Starvation Therapy/Phototherapy/Immunotherapy with Remarkably Enhanced Efficacy, Adv. Mater. 31 (2019) 1905271.
[37] E. Ju, K. Dong, Z. Chen, Z. Liu, C. Liu, Y. Huang, Z. Wang, F. Pu, J. Ren, X. Qu, Copper(II)–Graphitic Carbon Nitride Triggered Synergy: Improved ROS Generation and Reduced Glutathione Levels for Enhanced Photodynamic Therapy, Angew. Chem. Int. Ed. 55 (2016) 11467–11471.
[38] B. Ding, P. Zheng, P.a. Ma, J. Lin, Manganese Oxide Nanomaterials: Synthesis, Properties, and Theranostic Applications, Advanced Materials, 32 (2020) 1905823.
[39] G. Liu, J. Zhu, H. Guo, A. Sun, P. Chen, L. Xi, W. Huang, X. Song, X. Dong, Mo2C-Derived Polyoxometalate for NIR-II Photoacoustic Imaging-Guided Chemodynamic/Photothermal Synergistic, Therapy 58 (2019) 18641–18646.
[40] J.J. Pignatello, E. Oliveros, A. MacKay, Advanced Oxidation Processes for Organic Contaminant Destruction Based on the Fenton Reaction and Related Chemistry, Critical Rev. Environm. Sci. Technol. 36 (2006) 1–84.
[41] J. He, X. Yang, B. Men, D. Wang, Interfacial mechanisms of heterogeneous Fenton reactions catalyzed by iron-based materials: A review, J. Environ. Sci. 39 (2016) 97–109.
[42] Å. Björkbacka, M. Yang, C. Gasparrini, C. Leygraf, M. Jonsson, Kinetics and mechanisms of reactions between H2O2 and copper and copper oxides, Dalton Trans. 44 (2015) 16045–16051.
[43] H. Wang, Z. Zhang, H. Yin, Y. Wu, Synthesis of Cu2(OH)3Cl as facile and effective Fenton catalysts for mineralizing aromatic contaminants: Combination of σ-Cu-ligand and self-redox property, Appl. Catal. A 614 (2021) 118055.
[44] E. Ember, S. Rothbart, R. Puchta, R. van Eldik, Metal ion-catalyzed oxidative degradation of Orange II by H2O2 High catalytic activity of simple manganese salts, New J. Chem. 33 (2009) 34–49.
[45] Y. Sun, P. Tian, D. Ding, Z. Yang, W. Wang, H. Xin, J. Xu, Y.-F. Han, Revealing the active species of Cu-based catalysts for heterogeneous Fenton reaction, Appl. Catal. B 258 (2019) 117985.
[46] C.M. Lousada, A.J. Johansson, T. Brinck, M. Jonsson, Mechanism of H2O2 Decomposition on Transition Metal Oxide Surfaces, J. Phys. Chem. C 116 (17) (2012) 9533–9543.
[47] J.A. Cook, D. Gius, D.A. Wink, M.C. Krishna, A. Russo, J.B. Mitchell, Oxidative stress, redox, and the tumor microenvironment, Seminars Rad. Oncol. 14 (3) (2004) 259–266.
[48] D. Li, M. Hua, K. Fang, R. Liang, BSA directed-synthesis of biocompatible Fe3O4 nanoparticles for dual-modal T1 and T2 MR imaging in vivo, Anal. Methods 9 (21) (2017) 3099–3104.
[49] C. Hai, S. Li, Y. Zhou, J. Zeng, X. Ren, X. Li, Roles of ethylene glycol solvent and polymers in preparing uniformly distributed MgO nanoparticles, J. Asian Ceram. Soc. 5 (2) (2017) 176–182.
[50] Y. Fu, Q. Chen, M. He, Y. Wan, X. Sun, H. Xia, X. Wang, Copper Ferrite-Graphene Hybrid: A Multifunctional Heteroarchitecture for Photocatalysis and Energy Storage, Ind. Eng. Chem. Res. 51 (36) (2012) 11700–11709.
[51] M. Zhu, D. Meng, C. Wang, G. Diao, Facile Fabrication of Hierarchically Porous CuFe2O4 Nanospheres with Enhanced Capacitance Property, ACS Appl. Mater. Interfaces 5 (13) (2013) 6030–6037.
[52] I.-M. Tang, N. Krishnamra, N. Charoenphandhu, R. Hoonsawat, W.J.N.R.L. Pon-On, Biomagnetic of apatite-coated cobalt ferrite: a core–shell particle for protein adsorption and pH-controlled release, 6 (2011) 19.
[53] S.-H. Rhee, J.D. Lee, J. Tanaka, Nucleation of Hydroxyapatite Crystal through Chemical Interaction with Collagen, 83 (2000) 2890–2892.
[54] J. Hueso, J. Espinós, A. Caballero, J. Cotrino, A.J.C. González-Elipe, XPS investigation of the reaction of carbon with NO, O2, N2 and H2O plasmas, 45 (2007) 89–96.
[55] S.S. Maluf, P.A.P. Nascente, E.M. Assaf, CuO and CuO–ZnO catalysts supported on CeO2 and CeO2–LaO3 for low temperature water–gas shift reaction, Fuel Process. Technol. 91 (11) (2010) 1438–1445.
[56] E. Cano, C.L. Torres, J.M. Bastidas, An XPS study of copper corrosion originated by formic acid vapour at 40% and 80% relative humidity, Mater. Corros. 52 (2001) 667–676.
[57] K. Yuan, D. Lützenkirchen-Hecht, L. Li, L. Shuai, Y. Li, R. Cao, M. Qiu, X. Zhuang, M.K.H. Leung, Y. Chen, U. Scherf, Boosting Oxygen Reduction of Single Iron Active Sites via Geometric and Electronic Engineering: Nitrogen and Phosphorus Dual Coordination, J. Am. Chem. Soc. 142 (2020) 2404–2412.
[58] J. Yang, X. Wang, B. Li, L. Ma, L. Shi, Y. Xiong, H. Xu, Novel Iron/Cobalt-Containing Polypyrrole Hydrogel-Derived Trifunctional Electrocatalyst for Self-Powered Overall Water Splitting, Adv. Funct. Mater. 27 (2017) 1606497.
[59] X. Meng, D. Li, L. Chen, H. He, Q. Wang, C. Hong, J. He, X. Gao, Y. Yang, B. Jiang, G. Nie, X. Yan, L. Gao, K. Fan, High-Performance Self-Cascade Pyrite Nanozymes for Apoptosis-Ferroptosis Synergistic Tumor Therapy, ACS Nano 15 (3) (2021) 5735–5751.
[60] J. Shan, K. Yang, W. Xiu, Q. Qiu, S. Dai, L. Yuwen, L. Weng, Z. Teng, L. Wang, Cu2MoS4 Nanozyme with NIR-II Light Enhanced Catalytic Activity for Efficient Eradication of Multidrug-Resistant Bacteria, Small 16 (2020) 2001099.
[61] D. Wang, H. Wu, C. Wang, L. Gu, H. Chen, D. Jana, L. Feng, J. Liu, X. Wang, P. Xu, Z. Guo, Q. Chen, Y. Zhao, Self-Assembled Single-Site Nanozyme for Tumor-Specific Amplified Cascade Enzymatic Therapy, Angew. Chem. Int. Ed. 60 (2021) 3001–3007.
[62] E. Brillas, M.A. Baños, S. Camps, C. Arias, P.-L. Cabot, J.A. Garrido, R.M. Rodríguez, Catalytic effect of Fe2+, Cu2+ and UVA light on the electrochemical degradation of nitrobenzene using an oxygen-diffusion cathode, New J. Chem. 28 (2004) 314–322.
[63] T. Soltani, B.-K. Lee, Enhanced formation of sulfate radicals by metal-doped BiFeO3 under visible light for improving photo-Fenton catalytic degradation of 2-chlorophenol, Chem. Eng. J. 313 (2017) 1258–1268.
[64] H. Speisky, M. Gómez, F. Burgos-Bravo, C. López-Alarcón, C. Jullian, C. Olea-Azar, M.E. Aliaga, Generation of superoxide radicals by copper–glutathione complexes: Redox-consequences associated with their interaction with reduced glutathione, Bioorg. Med. Chem. 17 (2009) 1803–1810.
[65] M.R. Ciriolo, A. Desideri, M. Paci, G. Rotilio, Reconstitution of Cu, Zn-superoxide dismutase by the Cu(I).glutathione complex, J. Biol. Chem. 265 (1990) 11030–11034.
[66] J. Xu, R. Shi, G. Chen, S. Dong, P. Yang, Z. Zhang, N. Niu, S. Gai, F. He, Y. Fu, J. Lin, All-in-One Theranostic Nanomedicine with Ultrabright Second Near-Infrared Emission for Tumor-Modulated Bioimaging and Chemodynamic/Photodynamic Therapy, ACS Nano 14 (2020) 9613–9625.
[67] L. Flohé, The fairytale of the GSSG/GSH redox potential, Biochimica et Biophysica Acta (BBA), - General Subjects 1830 (2013) 3139–3142.
[68] M. Smeyne, R.J. Smeyne, Glutathione metabolism and Parkinson's disease, Free Radical Biol. Med. 62 (2013) 13–25.
[69] A. Meister, Glutathione metabolism and its selective modification, J. Biol. Chem. 263 (1988) 17205–17208.
[70] T.J. van 't Erve, B.A. Wagner, K.K. Ryckman, T.J. Raife, G.R. Buettner, The concentration of glutathione in human erythrocytes is a heritable trait, Free Radical Biol. Med. 65 (2013) 742–749.
[71] F. Bottino, M. Lucignani, A. Napolitano, F. Dellepiane, E. Visconti, M.C. Rossi Espagnet, L. Pasquini, In Vivo Brain GSH MRS Methods and Clinical Applications, Antioxidants 10 (2021).
[72] C.F. Wells, M.A. Salam, Hydrolysis of Ferrous Ions : a Kinetic Method for the Determination of the Fe(II) Species, Nature 205 (1965) 690–692.
[73] X. Shen, Z. Wang, X. Gao, Y. Zhao, Density Functional Theory-Based Method to Predict the Activities of Nanomaterials as Peroxidase Mimics, ACS Catal. 10 (2020) 12657–12665.
[74] L. Yu, Y. Chen, M. Wu, X. Cai, H. Yao, L. Zhang, H. Chen, J. Shi, Manganese Extraction Strategy Enables Tumor-Sensitive Biodegradability and Theranostics of Nanoparticles, J. Am. Chem. Soc. 138 (2016) 9881–9894.

[75] B. Yang, L. Ding, Y. Chen, J. Shi, Augmenting Tumor-Starvation Therapy by Cancer Cell Autophagy Inhibition, Advanced science (Weinheim, Baden-Wurttemberg, Germany), 7 (2020) 1902847.

[76] M.G. Vander Heiden, L.C. Cantley, C.B. Thompson, Understanding the Warburg Effect: The Metabolic Requirements of Cell Proliferation, Science 324 (5930) (2009) 1029–1033.

[77] L.-H. Fu, C. Qi, J. Lin, P. Huang, Catalytic chemistry of glucose oxidase in cancer diagnosis and treatment, Chem. Soc. Rev. 47 (17) (2018) 6454–6472.

[78] M.C. Ortega-Liebana, J.L. Hueso, R. Arenal, J. Santamaria, Titania-coated gold nanorods with expanded photocatalytic response Enzyme-like glucose oxidation under near-infrared illumination, Nanoscale 9 (5) (2017) 1787–1792.

[79] M.C. Ortega-Liebana, J.L. Hueso, S. Ferdousi, K.L. Yeung, J. Santamaria, Nitrogen-doped luminescent carbon nanodots for optimal photo-generation of hydroxyl radicals and visible-light expanded photo-catalysis, Diam. Relat. Mater. 65 (2016) 176–182.

[80] M. Sancho-Albero, N. Navascués, G. Mendoza, V. Sebastián, M. Arruebo, P. Martín-Duque, J. Santamaría, Exosome origin determines cell targeting and the transfer of therapeutic nanoparticles towards target cells, J. Nanobiotechnol. 17 (2019) 16.

[81] E. Rogatsky, H. Jayatillake, G. Goswami, V. Tomuta, D. Stein, Sensitive LC MS quantitative analysis of carbohydrates by Cs+ attachment, J. Am. Soc. Mass Spectrom. 16 (2005) 1805–1811.